RESEARCH ARTICLE | JUNE 10 2024

Wake-induced vibration suppression for a circular cylinder using a pair of jets

Baoshou Zhang (张宝收); Teng Long (龙腾); Ziyu Wang (王子玉); Wei Wang (王伟); Boyang Li (李博洋); Renhe Shi (史人赫)

Physics of Fluids 36, 067111 (2024)
https://doi.org/10.1063/5.0209230

View Online
Export Citation

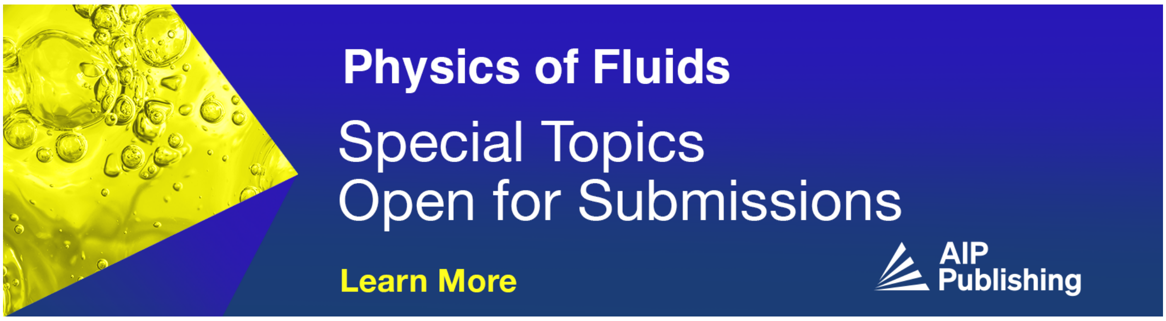

Physics of Fluids ARTICLE pubs.aip.org/aip/pof

Wake-induced vibration suppression for a circular cylinder using a pair of jets

Cite as: Phys. Fluids **36**, 067111 (2024); doi: 10.1063/5.0209230
Submitted: 19 March 2024 · Accepted: 25 May 2024 ·
Published Online: 10 June 2024

Baoshou Zhang (张宝收),[1] Teng Long (龙腾),[1,a)] Ziyu Wang (王子玉),[1] Wei Wang (王伟),[2] Boyang Li (李博洋),[3] and Renhe Shi (史人赫)[1]

AFFILIATIONS

[1]School of Aerospace Engineering, Beijing Institute of Technology, Beijing 100081, China
[2]Department of Civil and Environmental Engineering, The Hong Kong Polytechnic University, Kowloon, Hong Kong
[3]College of Electromechanical Engineering, Qingdao University of Science and Technology, Qingdao, Shandong, China

[a)]Author to whom correspondence should be addressed: tenglong@bit.edu.cn

ABSTRACT

The wake-induced vibration (WIV) presents significant challenges to the structural integrity of multi-cylinder configurations. To effectively alleviate this problem, a numerical simulation is conducted to assess the effect of an active control technique that uses two jets located at the shoulder region of a cylinder to suppress WIV in two-degree-of-freedom. The equations of motion for the WIV response are solved using the Newmark-β method. The Newmark-β method is employed to solve the equations of motion governing the WIV response. Three kinds of angular position (β) on WIV suppression are investigated in detail, including 30°, 60°, and 90°. The angular position β is defined as the angle between the injection angle and the horizontal line. When the angular position (β) is 30°, the maximum cross-flow amplitude ratio (CFAR) is reduced from 0.9 (uncontrolled) to 0.5 ($\beta = 30°$), a reduction of approximately 44%. On the contrary, the maximum CFARs remain approximately 1.0 for the case 3 ($\beta = 60°$) and case 4 ($\beta = 90°$). Especially for the case 4, the cylinder showed the galloping response after the upper branch region. Since the jets are positioned on the vibration cylinder shoulders, the vortexes caused by the jets are opposite to the main vortexes induced by the cylinder. As a consequence, the jets shred the main vortexes in the wake of the cylinder, which leads to the driving force of the vibration reduction. Therefore, the cylinder's WIV amplitude is significantly suppressed.

I. INTRODUCTION

The application of multi-cylinder structures is widespread across various engineering fields, encompassing cable-bearing bridges featuring parallel cables, clusters of marine risers, chimney clusters, and cooling tower clusters. Flow field between multi-cylinder structures can cause flow-induced vibrations (FIV). In particular, downstream of the cylinders, there are various forms of wake-induced vibration (WIV) including wake vortex-induced vibration (VIV), galloping, and flutter.[1,2] Among them, the VIV problems in marine risers have attracted attention. With the number of cylinder increment, flow interaction effects including wake interaction, proximity interaction, and their combination will occur. When the cylinders are positioned close to each other, these effects result in alterations in the attributes of the FIV response exhibited by the cylinders. In addition, the interaction of cylinders makes the flow field more complex, leading to a potentially more intense vibration response.[3] To alleviate the vibrations in the wake field and further improve the structural reliability of the marine riser groups, it has become more important to explore the cylindrical VIV suppression in the wake field.[4,5]

VIV suppression methods are currently a highly researched and prominent topic. The primary elements consist of methods for controlling vibrations, both actively and passively.[6–8] The implementation of active control approaches necessitates the provision of power input, as they rely on external energy sources to manipulate the flow and mitigate VIV. In contrast, passive control techniques do not require external power as they primarily rely on the geometry modifications of the structure to dampen or suppress VIV. Passive controls are simple to operate and cost-effective to control.[9,10] Wang *et al.* conducted research on the impact of a bionic surface resembling a colossal cactus for VIV suppression. In their study, the influence of different height ratios of the bionic surface for sixth ribs cases has been discussed.[11] Passive turbulence control experiments of circular obstacles are carried out by Chang *et al.* using surface roughness in a steady flow.[12] Ozkan Gokturk *et al.* conducted an experimental study where they altered the flow characteristics around a circular cylinder in shallow water by incorporating a porous outer cylinder. Their findings indicate that augmenting the porosity of the outer cylinder led to a diminished impact on the inner cylinder.[13] Among the various devices used to dampen vibrations, helical strakes are widely employed. The use of spiral columns has been experimentally proven to effectively minimize fatigue damage.[14,15] Sun *et al.*[16] adopted a flexible fishtail-like fairing as an FIV suppression, which has shown effectiveness in VIV suppression. In Ref. 17, tandem cylindrical VIV with flow-shape elastic mounting is simulated. The findings indicate that in numerous instances analyzed, there is a tendency for galloping response to manifest, resulting in significant oscillation magnitudes.

However, the effects of passive control techniques are often limited to a narrow range of conditions. On the other hand, optimal outcomes can be attained by flexibly adjusting the active control.[18] The numerical investigation, conducted by Mazzilli and Sanche,[19] aims to address the instability issue of a riser by developing an optimal control system that incorporates a linear quadratic regulator. This system is designed to stabilize the high-intensity oscillations experienced by a steel-catenary riser subjected to VIV. The vortex vibration of a cylinder is manipulated by Wan through the utilization of heat sources. The cylinder, which is elastically mounted and subjected to heating, experiences flow in alignment with the thermally induced buoyancy direction. They find that by increasing the Richardson number increment, it is possible to decrease the amplitude of VIV.[20] Lou *et al.* proposed the utilization of a Simulink co-simulation-based adaptive fuzzy sliding mode controller for actively controlling the VIV of the riser.[21] Xie *et al.* supposed a scheme and VIV of a cylinder accompanied by an appended filament, utilizing a penalty immersed boundary method.[22] Chizfahm presented a stability assessment for the VIV of a sphere and proposes a method to control VIV using base bleed actuation, which is beneficial to VIV suppression.[23]

Among the various active control techniques, using jets to suppress VIV is an effective method that has been widely investigated. It is feasible to manipulate the fluid dynamics around bluff bodies through the induction of a secondary flow (suction and blowing). In References 24 and 25, a numerical study is performed to evaluate the efficiency of an active control technique employing a duo of air jets situated at the shoulder regions of a circular cylinder for mitigating vortex-induced vibrations (VIV). To suppress the VIV, the air vortexes and bubbles effectively delay the vortex formation. In addition, they also study the effect of injection velocity on VIV. Kim and Choi examined the dispersion of flow pressure around a circular obstruction within a given range. At the lower and upper surfaces of the obstacle, the distributed force is found by the suction and blowing from the slots placed. The conditions that yield the highest drag reduction are identified.[26] A study is carried out by Wang *et al.* to numerically investigate the utilization of a pair of synthetic jets for active VIV control on a circular cylinder.[27] The active locking technique is less effective in suppressing VIV than the traditional eddy intensity reduction technique. In practical engineering applications, most of them are arrays of multiple columns arranged in series. Although the upstream cylinders block the impact of the flow, the shedding vortex will act on the surface of the downstream cylinders, thus enhancing the vibration of the downstream cylinders. Wang *et al.* first studied the wake-induced vibrations of three tandem semi-circular cylinders and found three wake interference patterns, which provided significant reference for this study.[28] Tang *et al.* investigated the effect of radius ratio on the motion of tandem cylinders. As the radius ratio increases, the motion of the downstream cylinder transitions from VIV to galloping.[29] Dongyang *et al.* found that placing a tuned NES parameters (mass, nonlinear stiffness, and damping) in tandem cylinders can also provide good suppression effects.[30] Xu *et al.* covered the surface of two tandem cylinders with helical strakes and found that the downstream cylinder may experience more severe fatigue damage in the cross-flow and in-line directions.[31]

To reduce the WIV responses for a circular cylinder, this paper explores the application of a dual water jet for active control. In the following sections, the problem description and setup are given in Sec. II. Section III presents the introduction of the computational model and approach. The outcomes concerning the WIV response, vortex shedding, and trajectories of the circular cylinder are discussed in Sec. IV. Section V describes the vibration suppression mechanism of the jets.

II. PROBLEM DESCRIPTION

In order to observe the influence of the jet on the WIV for the circular cylinder, the two-degree-of-freedom (2-DOF) WIV model with a pair of water jets is established as shown in Fig. 1. The model includes a stationary circular cylinder (left side) and a vibration circular cylinder (right side). The circular cylinder can vibrate freely in both the axial and transverse directions, while the oscillatory system consists of linear springs supporting the suspended cylinder along with damping within the system. Therefore, the oscillator can be described as a system consisting of a mass-spring-damper with two-degree-of-freedom (2-DOF). The oscillatory system parameters for numerical simulation are given in Table I.[32,33]

As shown in Fig. 2, this paper involves the immersion of two cylinders in a uniform water flow. The water jets, symmetrically positioned on both shoulders of the vibrating cylinder and centered around the rear stagnation point, are implemented. Each water jet uniformly injects with a steady velocity, covering a 2 mm width of the surface of the cylinder. This paper discusses the response of four cases at different velocities, and those cases are angular positions (β) of 30°, 60°, and 90° and uncontrolled.[34] The angular position is defined as the angle between the injection angle and the horizontal line. Four cases are applied to understand the influence of the water jet. Case 0 means isolated cylinder, case 1 means the downstream smooth cylinder, case 2 means the downstream cylinder with $\beta = 30^\circ$, case 3 means the downstream cylinder with $\beta = 60^\circ$, and case 4 means the downstream cylinder with $\beta = 90^\circ$. In addition, according to research of Zhu *et al.*, $U_{\text{jet}}/U_{\text{in}}$ is chosen 3.[24] U_{jet} represents the injection velocity of the water jets, and U_{in} represents the velocity of the ocean current.

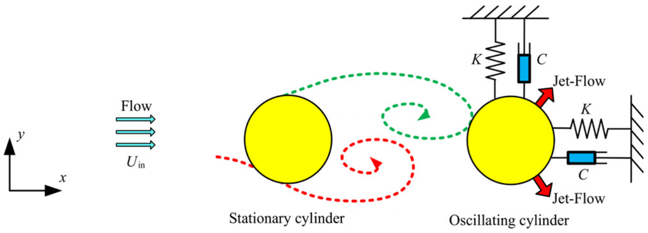

FIG. 1. Schematic of the 2-DOF wake-induced vibration model with a pair of jets.

TABLE I. VIV system parameters.

Denomination	Symbol	Value
Cylinder diameter	D (m)	0.1
Mass-ratio	m^*	2.6
Added mass coefficient	C_{add}	1.0
Natural frequency in water	f_n (Hz)	0.4
Spring stiffness	K (N/m)	179
Damping ratio	ξ	0.005
Width of Jet	H (mm)	2
Angular position	β (°)	30, 60, 90

III. NUMERICAL METHOD

A. Vibration equations and Newmark-β method

A mathematical model for the flow-induced motion (FIM) system is presented in this section. In this section, a mathematical model for the flow-induced motion (FIM) system is introduced. To depict the dynamics of the circular cylinder, a hybrid mass-spring-damper oscillator model (refer to Fig. 1) is employed.[35] The equation describing the motion in both the X and Y directions, considering two degrees of freedom, is as follows:

$$m\ddot{x}+C_{\text{total}}\dot{x}+Kx = F_{\text{fluid},x}(t), \tag{1}$$

$$m\ddot{y}+C_{\text{total}}\dot{y}+Ky = F_{\text{fluid},y}(t), \tag{2}$$

where m, x, y, $F_{\text{fluid},x}(t)$, and $F_{\text{fluid},y}(t)$ are the circular cylinder mass, the displacement, and the fluid force in X and Y directions, respectively. $C_{\text{total}}=\xi_{\text{total}}\left(2\sqrt{\text{m}\cdot\text{K}}\right)$ is the total damping.

For this work, the solution to the mass-spring-damper oscillator model is obtained by employing the Newmark-β method. The adopted method has been extensively utilized in the field of structural dynamics to tackle the mathematical representation given by Eqs. (1) and (2).[36,37] The Newmark-β method has been adopted in our previous research, and in this paper, we have updated the writing errors. Consider cross-flow vibration as an example, the Newmark-β method can express the displacement, y, velocity, $\dot{y}$, and acceleration, $\ddot{y}$, in the formulated manner as

$$y_{\text{t}+\Delta\text{t}}=(y_t+\dot{y}\,\Delta t)+\left[\left(\frac{1}{2}-\beta\right)\ddot{y}_{\text{t}}+\beta\,\ddot{y}_{\text{t}+\Delta t}\right]\Delta t^2, \tag{3}$$

$$\dot{y}_{\text{t}+\Delta\text{t}}=\frac{\gamma}{\beta\,\Delta t}\left(y_{t+\Delta t}-y_t\right)+\left(1-\frac{\gamma}{\beta}\right)\dot{y}_t+\left(1-\frac{\gamma}{2\beta}\right)\ddot{y}_t\Delta t, \tag{4}$$

$$\ddot{y}_{\text{t}+\Delta\text{t}}=\frac{1}{\beta\,\Delta t^2}\left(y_{\text{t}+\Delta\text{t}}-y_t\right)-\frac{1}{\beta\Delta t}\dot{y}_{\text{t}}-\left(\frac{1}{2\beta}-1\right)\ddot{y}_{\text{t}}, \tag{5}$$

where the time level is denoted by the subscript t or $t+\Delta t$ in this method. The adjustable weighting constants, γ and β, have been studied in Refs. 38 and 39. In the Newmark-β method discussed here, the values chosen for γ and β are 0.5 and 0.25, respectively. These values guarantee both unconditional stability and second-order accuracy for non-dissipative linear systems.

Considering Eq. (2) at time $t+\Delta t$, we have

$$M\,\ddot{y}_{\text{t}+\Delta\text{t}}+C_{\text{total}}\,\dot{y}_{\text{t}+\Delta\text{t}}+K\,y_{\text{t}+\Delta\text{t}}=F_{\text{fluid},y}(t)_{\text{t}+\Delta\text{t}}. \tag{6}$$

The substitution of Eqs. (3)–(5) in Eq. (6) gives

$$[\bar{K}]\,y_{\text{t}+\Delta\text{t}}=[\bar{F}], \tag{7}$$

where

$$[\bar{K}]=K+\frac{1}{\beta\,\Delta t^2}M+\frac{\gamma}{\beta\,\Delta t}\,C_{total}, \tag{8a}$$

$$[\bar{F}]=F_{fluid,y}(t)_{\text{t}+\Delta\text{t}}+\left[\frac{1}{\beta\,\Delta t^2}\,y_t+\frac{1}{\beta\,\Delta t}\,\dot{y}_t+\left(\frac{1}{2\beta}-1\right)\ddot{y}_t\right]M$$
$$+\left[\frac{\gamma}{\beta\,\Delta t}\,y_t+\left(\frac{\gamma}{\beta}-1\right)\dot{y}_t+\left(\frac{\gamma}{2\beta}-1\right)\Delta t\ddot{y}_t\right]C_{total}). \tag{8b}$$

The resolution of Eqs. (4), (5), and (7) is facilitated by computer algorithms that have been previously employed in our earlier research.[40] Further details regarding the specific implementation of this methodology are not provided in this discussion.

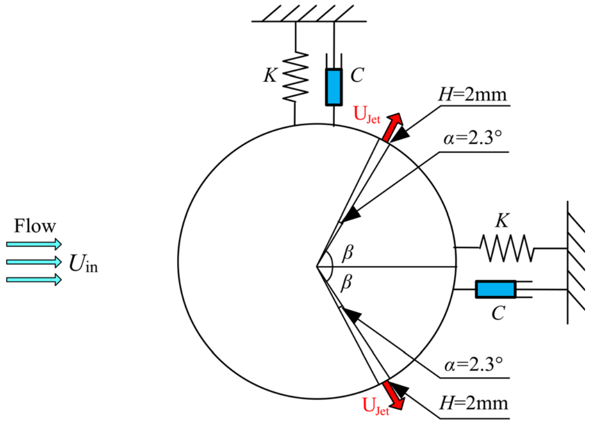

FIG. 2. Circular cylinder schematic with jets.

B. Two-way FSI simulation

VIV is a typical FSI (fluid–structure interaction) problem. The numerical simulation procedure for VIV in this study involves two components: resolving fluid forces and addressing the motion equation. In general, the simulation flow chart is presented in Fig. 3. The governing equations and computational domains have been extensively addressed in our previous research,[40] so are not provided here. The numerical method is briefly introduced as follows:

1. The foundation of motion simulation lies in acquiring fluid force. For this study, the CFD software Fluent was utilized with the RANS (Reynolds-averaged Navier–Stokes) equations and SST (shear stress transport) k-ω turbulence model to obtain results.[41,42]
2. The UDF (user-defined functions) module enables bidirectional communication between fluid force and circular cylinder motion. By employing the Newmark-β method, a second-order linear differential equation [Eqs. (1) and (2)] is solved. The UDF module integrates C++ computer algorithms to compute various parameters such as the current vibration velocity V_{t} and displacement. These values are then utilized to update the position of the cylinder within Fluent by modifying the grid based on displacement information.

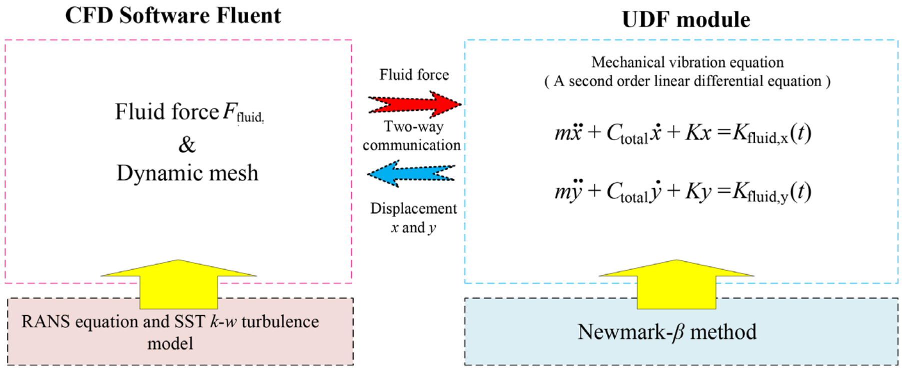

FIG. 3. Two-way FSI simulation process for VIV with mass-spring-damper system.

C. Computational Domain and Grid

Figure 4 shows the computational domain including the VIV system. The computational domain extends 20 times the cylinder diameter in the lateral direction and 40 times in the longitudinal direction. As shown in Fig. 4, two cylinders of the same size are set up in the computational domain; the left side remains constant, while the right side exhibits vibration. The core area for the motion of the vibrating cylinder (right side one) is achieved by using the layering method (dynamic grid method). This involves dividing the slideway into two sections, *A* and *B*, which are strategically positioned along both the cross-flow and in-flow directions of the vibration cylinder.

Four boundary conditions, namely, inlet (velocity-inlet), sidewall, outlet (pressure-outlet), and cylinder-wall (no-slip wall), are set. The boundary layer is set on two cylinders to improve the accuracy. In Fig. 5, the global grid uses a quadrilateral design scheme. In general, the hydrodynamic environment around the cylinder is complex. The mutual coupling of water jets and vortices further increases the complexity of the flow field around the cylinder. In order to accurately simulate the flow field around the cylinder, the prism layer is applied to the wall of the cylinder and jets. The growth rate is 1.2 and prism layer is 16. Based on the requirements of the SST k-ω turbulence model, the value of dimensionless wall distance (y+) should be less than 1. Therefore, the height of the first layer mesh is 8×10^{-7} m. The grooves are located at the two shoulders of the vibration cylinder. The grooves are the key to achieving the jet flow, so the grid near grooves is optimized (Fig. 6).

D. Numerical method validation

Since there are no practical experiments and numerical examples that fit perfectly with this study, the results of Jauvtis and Kang are chosen as a benchmark example to test the numerical method.[43–45] The precision of the numerical model has been verified against the previous results for the vibration of a smooth cylinder. The VIV response region is characterized by three branches, namely, the initial branch, upper branch, and lower branch. In the initial and upper branches, even if there is a small non-overlap, the present outcome exhibits resemblance to findings from other studies. The amplitude ratio in the current study is slightly higher than that of Kang's study in the lower branch. The magnitude of the observed amplitude ratio slightly exceeds that reported by Kang in the lower branch. In the VIV response region, the numerical method can clearly show the three branches. Therefore, the numerical method in this paper is acceptable. In the region where VIV response occurs, the three branches are effectively displayed using the numerical method. As such, this paper's numerical method is deemed appropriate.

Time records for the cross-flow amplitude ratio (CFAR) and trajectory for two tandem cylinders are given in Fig. 7. The angular position is 60°, and the reduced velocity is 7.0. The amplitude ratio

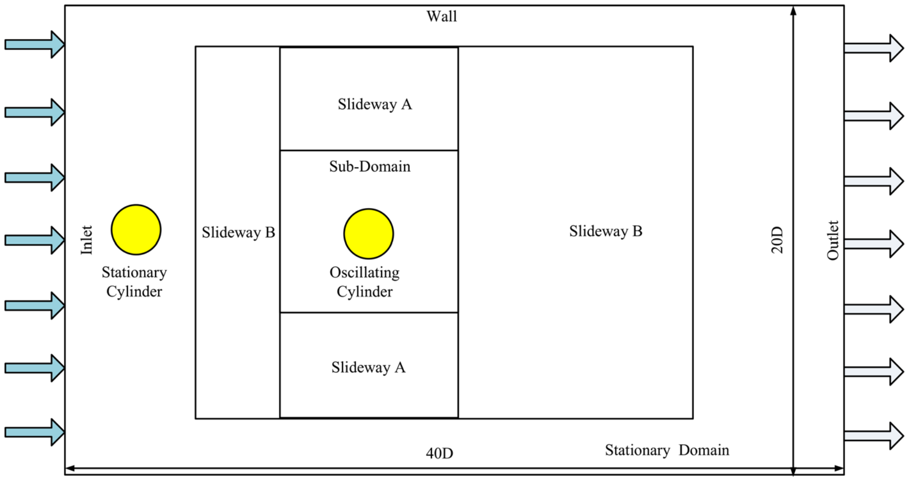

FIG. 4. Computational domain.

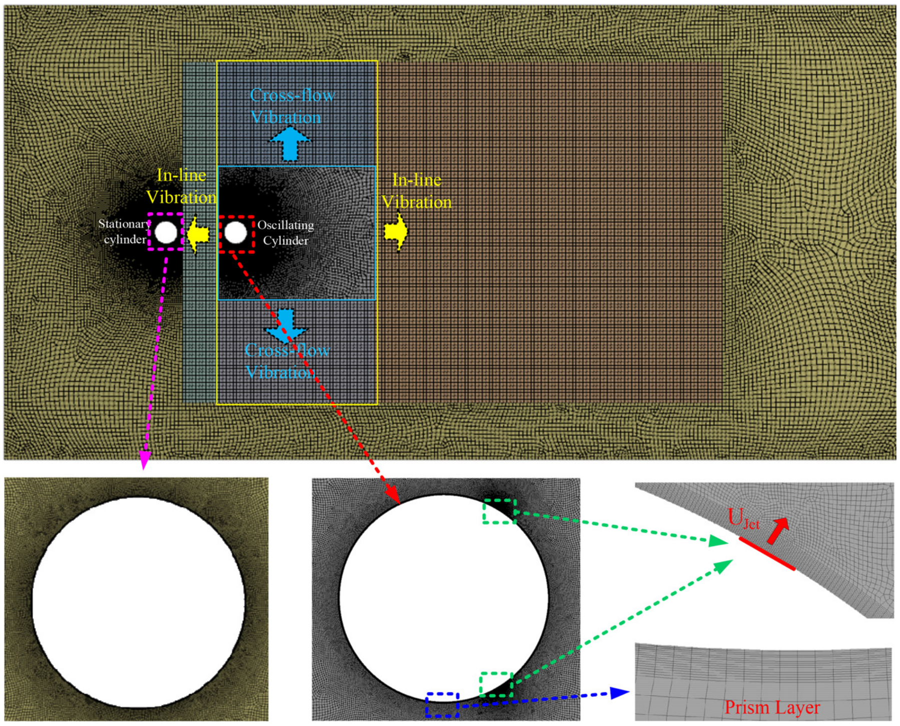

FIG. 5. Global grid, local grid near the cylinder, and boundary layer grid near the grooves.

without control undergoes regular sinusoidal fluctuation, and the maximum CFAR and trajectory reach 1.3 and 0.13, respectively. The instability of the fluctuation arises when the cylinder is fitted with a pair of water jets. In general, compared to the no jet control, the CFAR is decreased to 0.5. It indicates that the water jets influence the VIV. Furthermore, the range of vibration trajectory has been reduced under the water jet control.

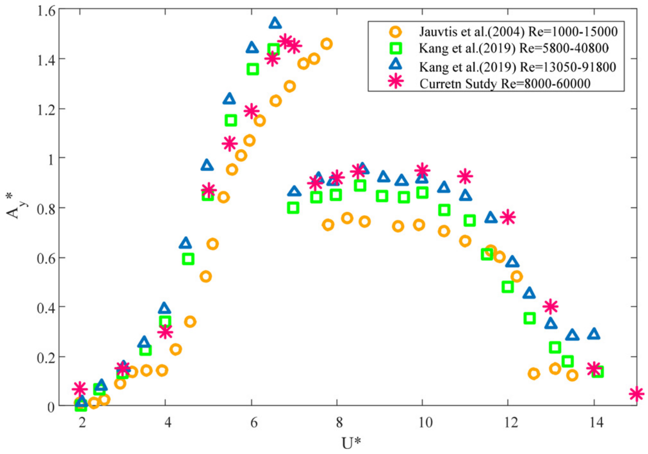

FIG. 6. Comparison of the numerical results from the current study and the experimental results from Jauvtis and Williamson and Kang *et al.* for the VIV amplitudes at $m* = 2.6$ and $\xi = 0.005$.

IV. RESULTS AND DISCUSSION

A. VIV amplitude and frequency responses

Figure 8 shows the CFARs ($A_y^* = A/D$) for the isolated cylinder (case 0), downstream smooth cylinder (case 1), and downstream cylinder of jet at $U_{\text{jet}}/U_{\text{in}} = 3$ with diffident angular positions (case 2, 30°, case 3, 60°, and case 4, 90°). The data are derived from the average values of A_y^* over the last ten cycles of the time historical curves. In Fig. 8, the identification of VIV response regions typically involves the utilization of four branches, namely, the initial branch, upper branch, lower branch, and desynchronization. Figure 9 is about vortex shedding frequency ratios ($f_y^* = f/f_{n,water}$), and the determination of vortex shedding frequency can be achieved by employing the fast Fourier transform (FFT). The lock-in phenomenon occurs when the vortex shedding frequency is close to the natural frequency. The occurrence of the lock-in phenomenon arises when the natural frequency closely aligns with the vortex shedding frequency.

In the region of the initial branch, cases 0–4 can be identified by their distinct characteristics of having low frequency ratios and amplitude ratios. The frequency ratios of vortex shedding in the cases are below 1.0, and the frequency ratio of case 2 is higher. The CFARs are less than 0.6. The frequency ratios of vortex shedding and all cases increase with the reduced velocity increment. Under $U^* = 4$, compared with case 1, the reduction in the frequency ratio of vortex shedding and case 2 is observed.

For the upper branch region, the CFARs of all cases begin to increase more rapidly than the initial branch until they reach the peak. The CFAR of case 0 is higher, and its peak value is 1.5. The maximum CFAR for case 2 is about 0.5, and it is about 0.9 for case 1, which is reduced by 44% compared with that of case 1. On the contrary, the

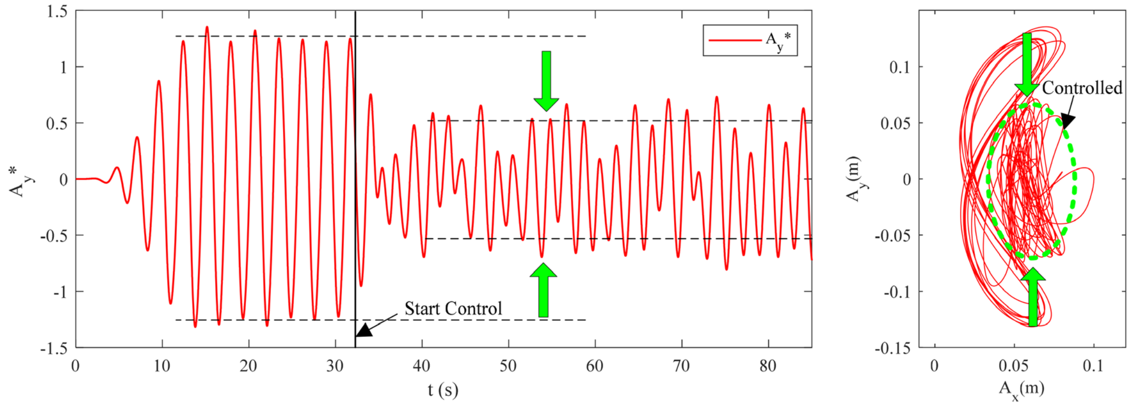

FIG. 7. VIV suppression for tandem cylinders using a pair of water jets ($\beta = 60^\circ$): CFAR (A_y*) and trajectory (A_y, A_x) ($U* = 7.0$).

maximum CFARs are about 1.0 in cases 3 and 4, which exhibit a slight increase in comparison with case 1. The frequency ratios of vortex shedding in cases 1–4 exhibit a gradual increase, eventually surpassing the value of 1.0. The frequency ratio of vortex shedding in case 0 remains stable at approximately 1.0 and does not exhibit a significant increase with an increase in velocity ratio.

In the lower branch region, all cases are present in a state of stability within the lock-in region. The VIV responses exhibit a contrasting pattern of high amplitude ratio and high frequency ratio compared to the initial branch region. The amplitude ratio of case 2 is lower, and the stability of the CFAR remains at approximately 0.3, exhibiting a reduction of around 67% compared to case 1's maximum CFAR. Meanwhile, the CFAR of case 3 is approximately 0.4, exhibiting a significant reduction of 56% compared to case 1 under the same conditions. However, case 4 shows galloping phenomenon, and the amplitude rapidly increases with reduced velocity increment. The frequency ratios of vortex shedding in case 2 remain consistent at approximately $St = 0.2$, while the CFARs also exhibit stability. When the vortex shedding frequency coincides with the natural frequency, the cylinder experiences resonance, which has also been interpreted by some scholars as a lock-in phenomenon.[35,36] Then, the vibration will be enhanced, and the amplitude will be increased. The vortex shedding frequency ratios of case 4 are about 1, corresponding to the natural frequency. Thus, amplitude ratio of case 4 is significantly higher than the other conditions.

In the region of desynchronization, all cases exhibit VIV responses with a low amplitude ratio, except for case 4. This indicates that the high Reynolds number region effectively suppresses the amplitude responses. The frequency ratios of vortex shedding in cases 0–3 are high, while case 4 is lower.

B. VIV responses and vortex shedding patterns in different branches

1. Initial branch

To further gain the fluid dynamics of WIV using a pair of jets, the analysis is extended to include the amplitude ratio of cross-flow, lift coefficient, and patterns of vortex. About certain kinds of different cases, four typical reduced velocities ($U^* = 4$, 7, 11, and 14) have been chosen for further analysis of the VIV responses. Figure 10 shows the cylinder VIV responses (cases 1, 2, 3, and 4) under $U^* = 4$ in the initial branch. In addition, Fig. 11 shows the vortex patterns. When $U^* = 4$ (Fig. 10), the maximum CFAR is approximately 0.3 in case 1. The maximum CFAR is only less than 0.2 in case 2. The maximum case 3

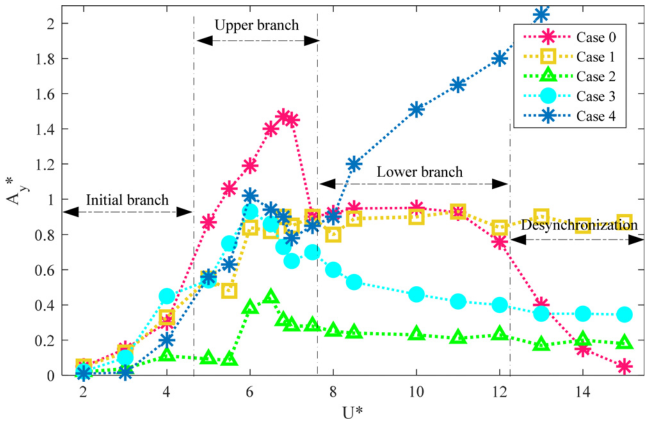

FIG. 8. Comparison of the amplitude responses of the circular cylinders.

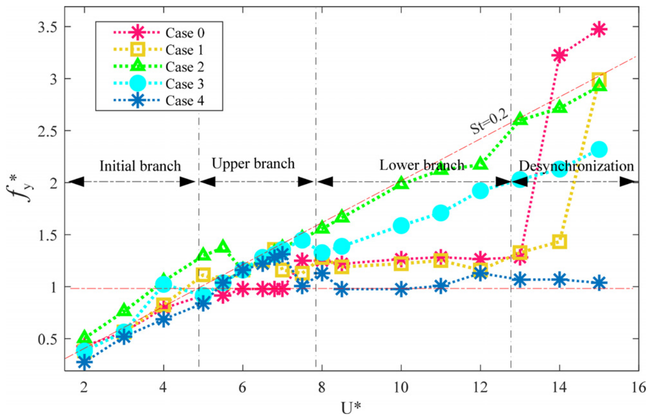

FIG. 9. Comparison of the frequency responses of the circular cylinders.

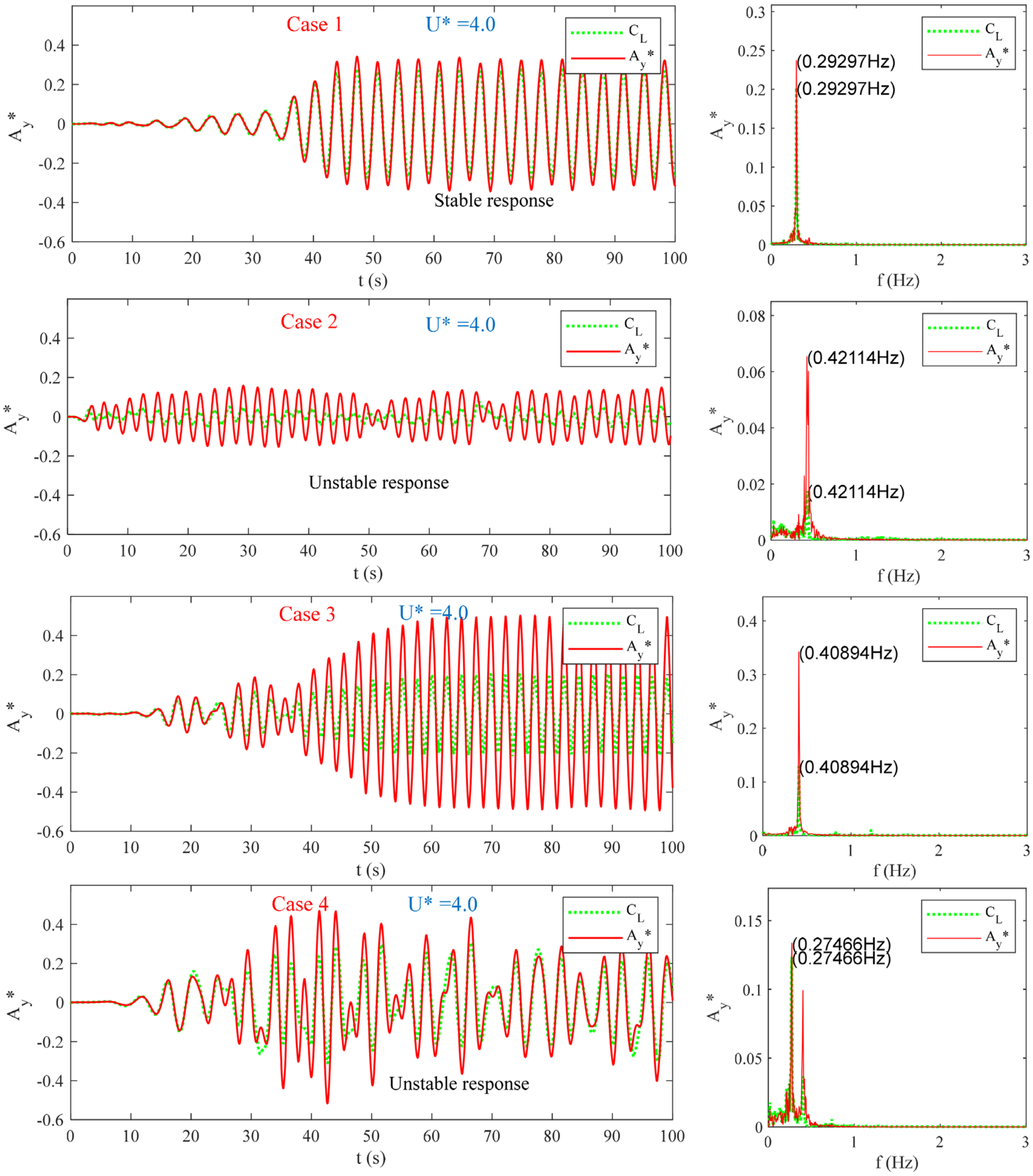

FIG. 10. The time histories of VIV responses of the cylinders ($U* = 4.0$).

is about 0.5, and it is higher than without control (case 1). In addition, the CFAR in case 4 shows an unstable vibration response. Here, the lift coefficient is only used to describe the trend. The lift coefficient and cross-flow amplitude exhibit consistent dominant frequencies. The lift coefficient exhibits dominant frequencies for cases 1–4, which are 0.292 97, 0.421 14, 0.408 94, and 0.274 66 Hz, respectively. The vortexes generated by the stationary cylinder (left side one) are attached to the surface of the vibrating cylinder for cases 2 and 3, as depicted in Fig. 11. The surface of the vibrating cylinder receives vortex shedding from the stationary cylinder for cases 1 and 4. As shown in figure, the jet disturbs the inner side of the shear layer, resulting in the formation of a new vortex in the opposite direction to the nearby vortex, destroying the original vortex shedding. In addition, as the jet is deflected downstream by the incoming flow, a pair of vortexes are generated on either side of the jet. The different vortex patterns associated with specific VIV or FIM (flow-induced motion) regimes have been named as the S mode or P mode, where S and P stand for a single and pairs of vortices shed in one cycle. The vortex patterns observed in all instances exhibit 2 P modes, with the exception of case 1 (without control). There are two pair vortexes behind the cylinder, between 0 and 0.3 m.

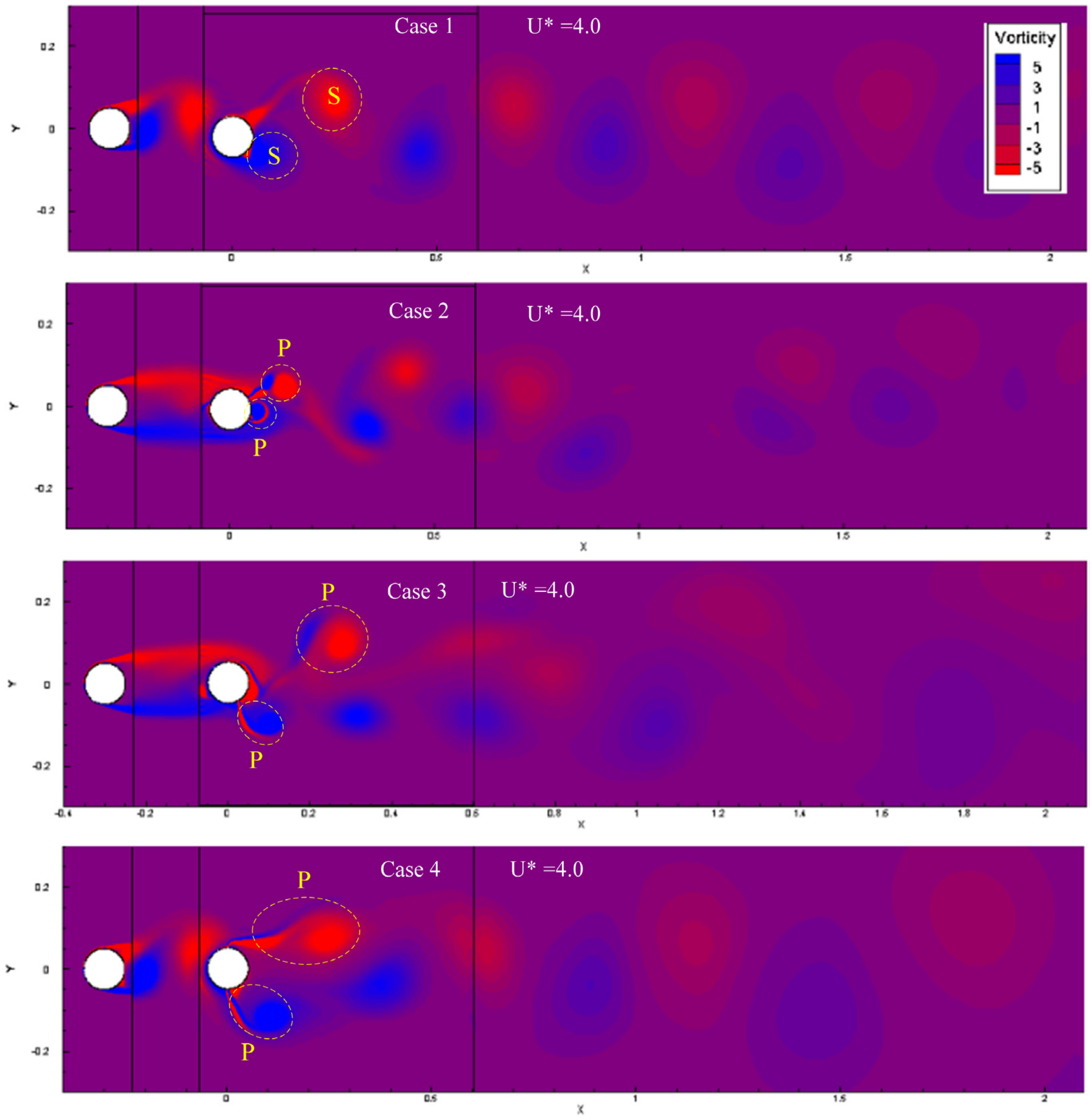

FIG. 11. The vortex patterns of the cylinders ($U* = 4.0$).

The cylinder sequentially sheds two vortexes from its rear, and the vortexes in each pair rotate in opposite directions. In addition, there are two vortexes behind the cylinder for case 1, its vortex patterns of 2S mode. Notably, the vortex is no longer covering the cylinder walls for case 4.

2. Upper branch

In the upper branch, Fig. 12 illustrates the temporal evolution of VIV exhibited by the cylinder (cases 1, 2, 3, and 4) under $U^* = 7$. In addition, the vortex patterns are depicted in Fig. 13. When $U^* = 7.0$, the maximum amplitudes of ratio cross-flow for cases 1, 3, and 4 are about 1.0. The maximum CFAR for case 2 is approximately 0.4, exhibiting a significant reduction of 60% compared to case 1. It is noteworthy that case 1 shows an unstable amplitude ratio at the 40 s moment, and case 3 shows an unstable amplitude ratio at the 40 and 60 s moment. The CFARs in all cases exhibit elevated values in the upper region when compared to the initial region, respectively. The lift coefficient in case 1 exhibits a dominant frequency of 0.952 15 Hz, while the CFAR demonstrates a dominant frequency of 0.463 87 Hz. However, the dominant frequency of the lift coefficient and CFAR for cases 2–4 is similar, with values of 0.549 32, 0.543 21, and 0.5249 Hz. In Fig. 13, the vortex pattern is the 2P mode for all cases. This phenomenon is caused by the number of shedding vortexes increasing with the higher flow rate in one cycle so that the 2S mode becomes 2P mode. In addition, because of the water jet, the position of the vortex shedding is shifted to a position farther away on both sides of the cylinder.

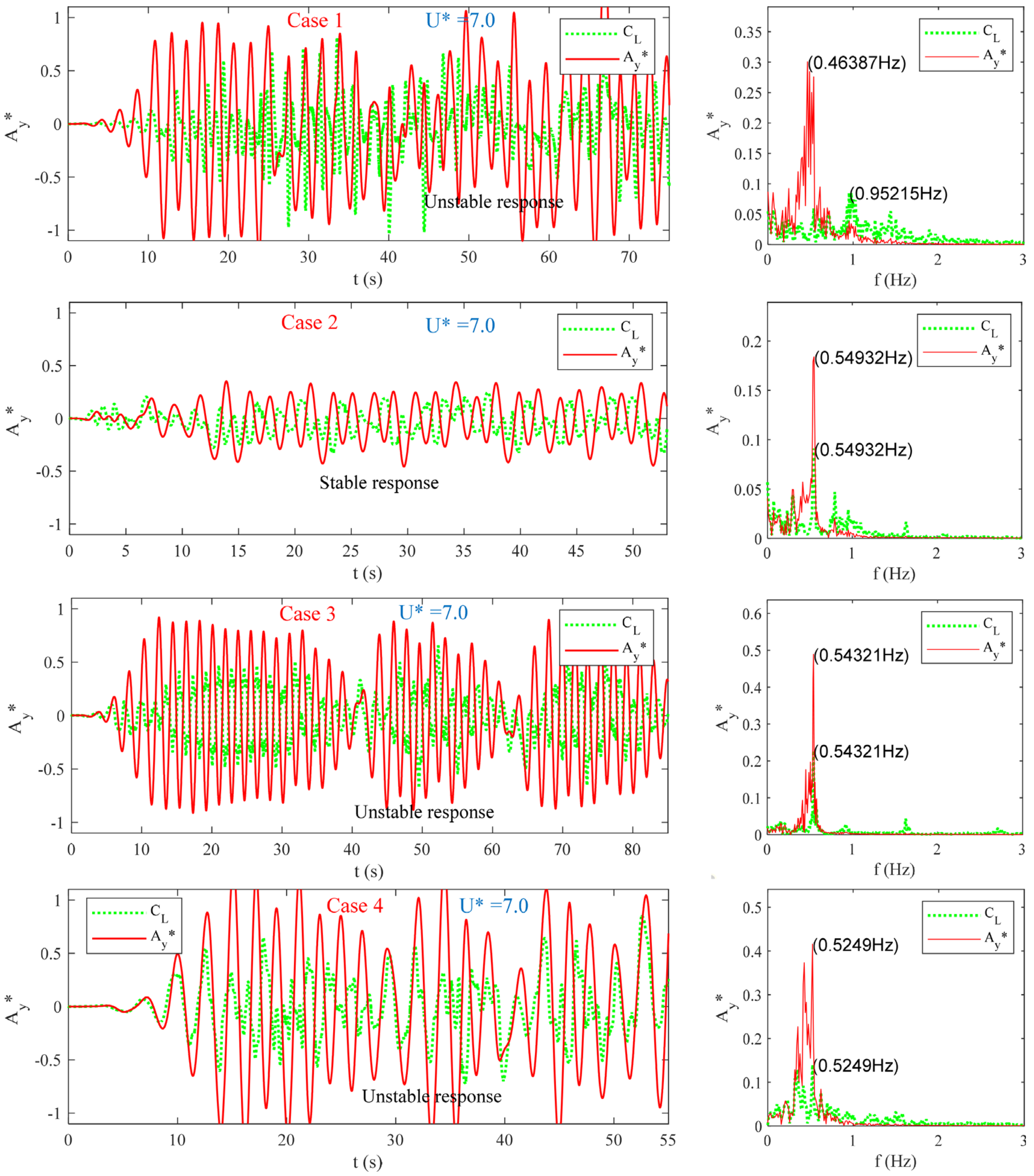

FIG. 12. The time histories of VIV responses of the cylinders ($U* = 7.0$).

3. Lower branch

In the lower branch, Fig. 14 illustrates the VIV responses for the cylinder (cases 1, 2, 3, and 4) under $U^* = 11$. In addition, Fig. 15 shows the vortex patterns. When $U^* = 11$ (Fig. 14), the maximum CFAR for case 1 is about 1.5, that is, the higher velocity leads to an increase in the amplitude of the cylindrical vibration compared to the upper branch. The maximum CFAR for case 2 is approximately 0.3, which is reduced by 75% compared with case 1, and the jets provide significant suppression of cylindrical wake vibrations. The maximum CFAR for case 3 is approximately 1.0, which is decreased by 33% in comparison with case 1. However, it is 2.0 for case 4, which is increased by 33% compared with case 1, and this indicates that the 90° jet in the lower branch promotes cylindrical vibration. The lift coefficient and CFAR for case 2 exhibit a consistent dominant frequency of 0.848 39 Hz. However, the dominant frequency of the lift coefficient and CFAR in cases 1, 3, and 4 is not constant, and the dominant frequency values of the CFAR are bigger than the lift coefficient, respectively. The dominant frequency of the CFAR for cases 1, 3, and 4 is about 0.5, 0.683 59, and 0.402 83 Hz, respectively. All cases except case 4 exhibit vortex

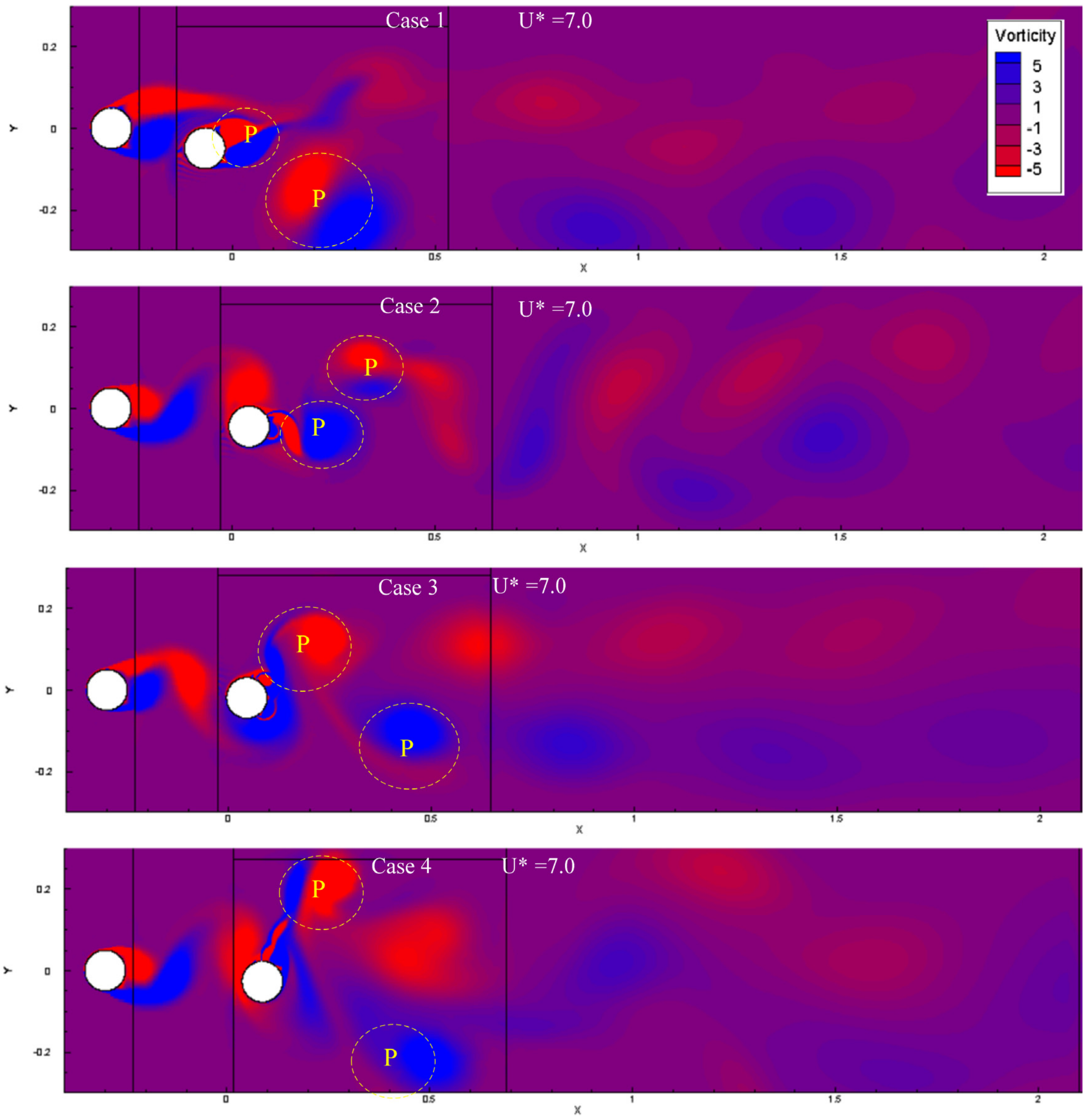

FIG. 13. The vortex patterns of the cylinders ($U* = 7.0$).

patterns in the 2P mode in Fig. 15, with two pairs of vortices located at a significant distance from the cylinder. In addition, as the cylinder amplitude is large, this results in a long vortex stroke for the cylinder shedding. With U^* increasing, among the cylinder of case 4 sheds more vortexes, the vortex pattern is the 4P mode. The increase in the number of vortices can be one of the reasons for the increase in the lift coefficient. Thus, the 90° jet in the lower branch promotes cylindrical vibration.

4. Desynchronization

In desynchronization, Fig. 16 illustrates the VIV responses of the cylinder (cases 1, 2, 3, and 4) under $U^* = 14$. In addition, Fig. 17 shows the vortex patterns. When $U^* = 14$, for case 1, the curve of the CFAR is quickly convergence and stable, and the maximum CFAR is approximately 0.8. Cylindrical vibrations become unstable for cases 2 and 3. The maximum CFAR is more than 2.0 for case 4, which is increased by 50% compared with case 1. This indicates that the 90° jet promotes cylindrical vibrations in desynchronization. The lift coefficient and CFAR exhibit distinct dominant frequencies in cases 1, 3, and 4. However, the lift coefficient and CFAR for case 2 exhibit a consistent dominant frequency of 1.0864 Hz. Case 2 has the lowest vibration amplitude but the highest vibration frequency. In Fig. 17, the distribution of high velocity flow areas has similar characteristics in cases 1–3. The vortex patterns for all cases are 2P mode. However, the amplitude of the 90° jet cylinder in the high flow velocity region is greater than that in case 1. The vortex pattern of the case 4 is 4P. It can be observed

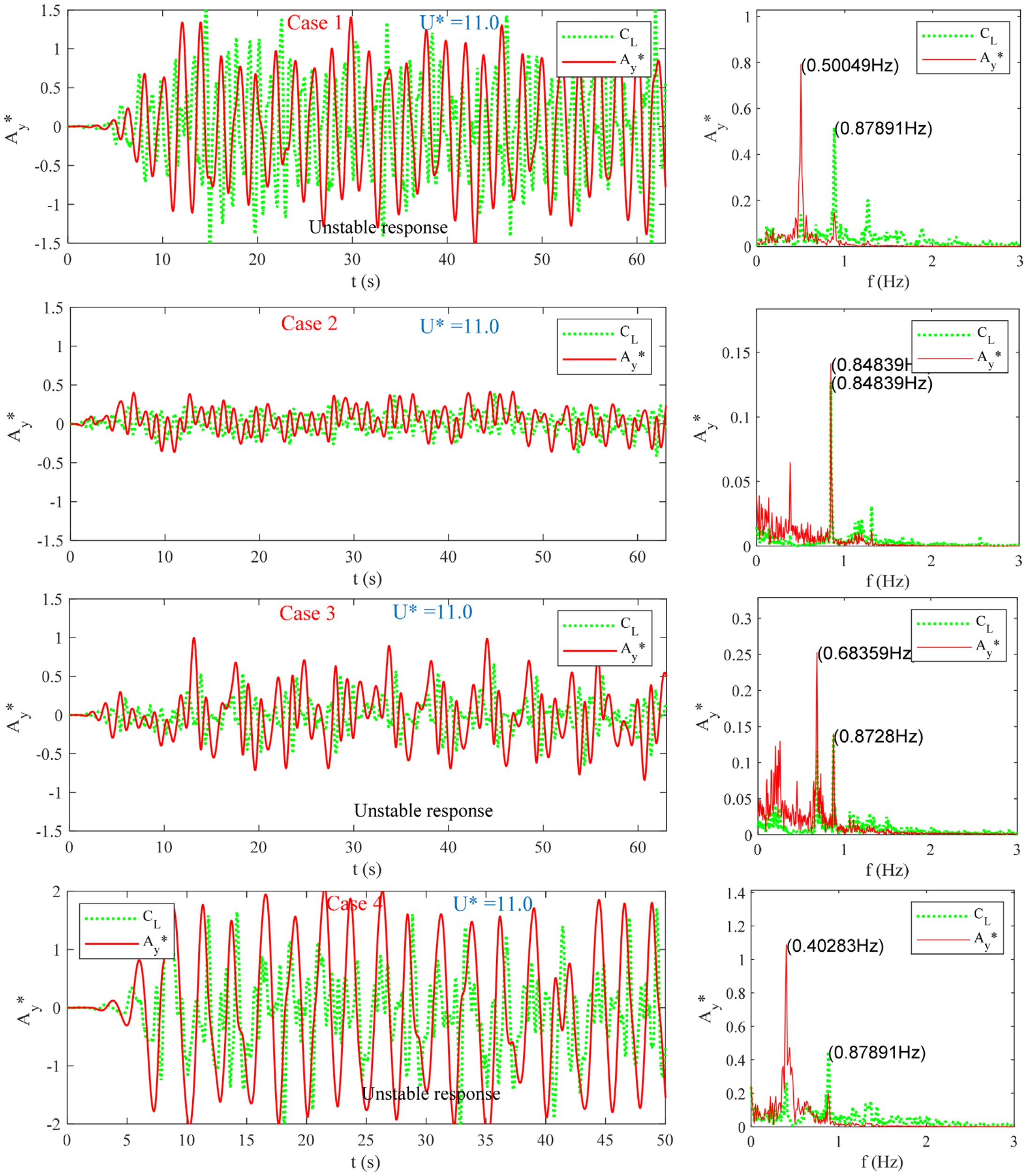

FIG. 14. The time histories of VIV responses of the cylinders ($U* = 11.0$).

by the vortices at the same location in the wake that the vortex in case 4 is stronger than the other cases. In addition, four examples are shown in Fig. 17 where the vortex shedding wakes all become longer in desynchronization. The lift coefficient and CFAR for case 2 exhibit a consistent dominant frequency of 1.0864 Hz.

C. Trajectories in different branches

Figure 18 shows the vibration trajectories of the circular cylinder (cases 0, 1, 2, 3, and 4) under $U^* = 4.0$, 7.0, 11.0, and 14.0. For case 0, the vibration trajectory is the one-shaped trajectory. Compared to case 0, case 1 is an uncontrolled cylindrical vibration trajectory in the wake. The cylinder trajectory expands in the in-flow direction, and the vibrations in the cross-flow direction become chaotic, which suggests that a more intense VIV response in the wake flow appears. The vibration trajectories of all cases exhibit the one-shaped trajectories under $U^* = 4.0$. With the reduced velocity increment, there is an initial increase, followed by a subsequent decrease in the range of motion trajectory for case 1. Under $U^* = 7.0$, 11, and 14, the ranges of vibration trajectory for case 2 are ($-0.04\,\text{m} < A_y < 0.04\,\text{m}$; $-0.03\,\text{m} < A_x$

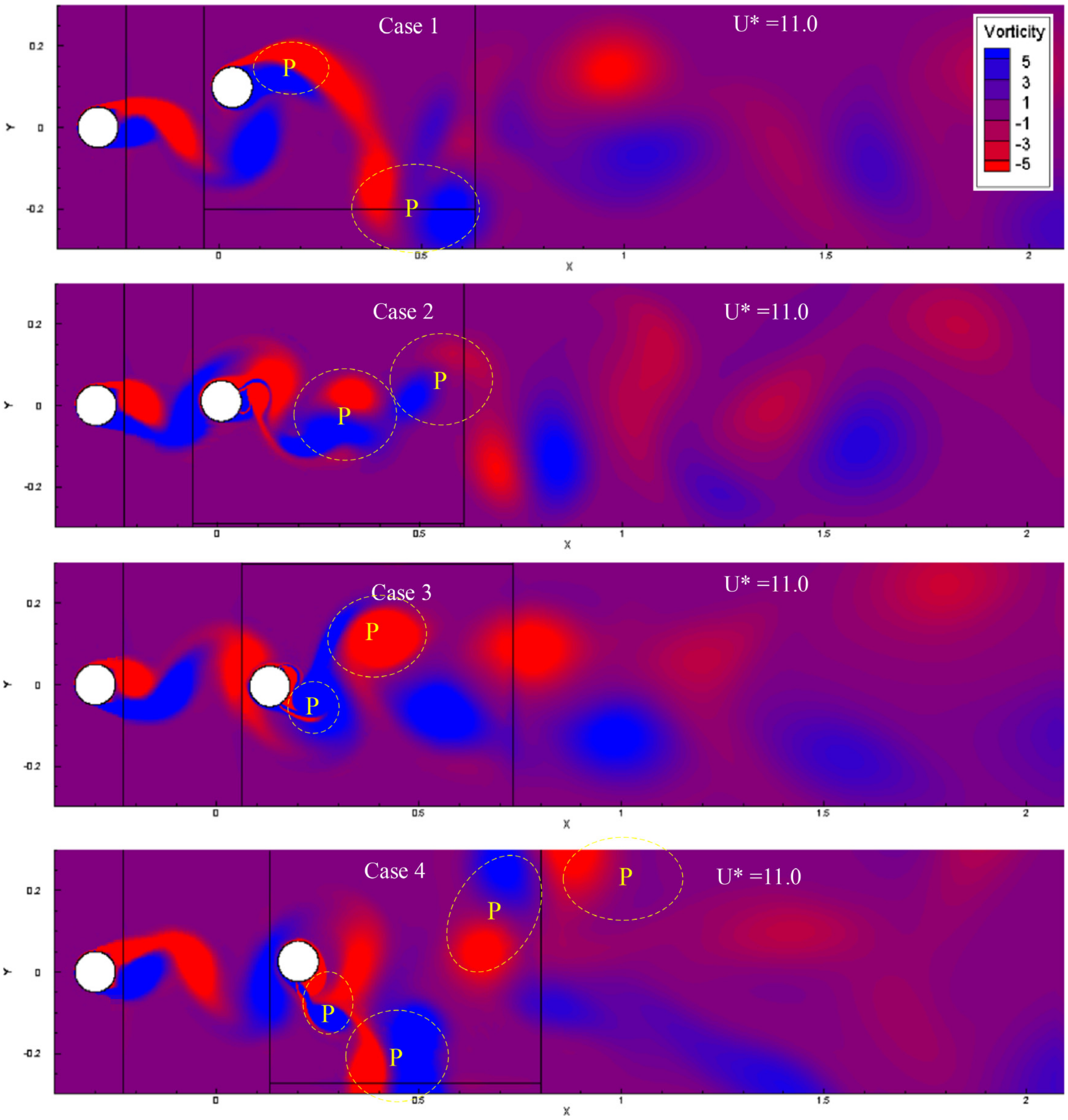

FIG. 15. The vortex patterns of the cylinders ($U* = 11.0$).

< 0.06 m), (-0.05 m $< A_y < 0.05$ m; -0.05 m $< A_x < 0.05$ m), and (-0.06 m $< A_y < 0.09$ m; -0.09 m $< A_x < 0.06$ m), respectively. All reduced velocities of case 2 are dot-shaped except $U^* = 4.0$. Compared to the cylindrical vibration response in case 1, the cylindrical amplitude ratio is significantly smaller and the cylindrical vibration response is suppressed. For case 3 under $U^* = 7.0$, 11, and 14, the range of vibration trajectory is (-0.07 m $< A_y < 0.09$ m; 0.01 m $< A_x < 0.06$ m), (-0.1 m $< A_y < 0.1$ m; 0.05 m $< A_x < 0.16$ m), and (-0.14 m $< A_y < 0.11$ m; 0.09 m $< A_x < 0.25$ m), respectively. The vibration trajectory shows an obvious one-shaped trajectory for case 4. Compared to the cylindrical vibration response in case 1, the cylindrical amplitude ratios at $U^* = 11.0$ and $U^* = 14.0$ are significantly bigger and the cylindrical vibration response is not suppressed.

V. VIBRATION SUPPRESSION MECHANISM

A. Pressure distribution on the cylinders

Following the above-mentioned discussion, a comprehensive analysis is provided to elucidate the impact of cylinders equipped with jets on the VIV responses. Nevertheless, additional analysis is required to examine the impact of the jet on the VIV response. In Fig. 19, the pressure contours surrounding the fixed and vibrating cylinders are shown. As an example, for $U^* = 7.0$, pressure contours are given for

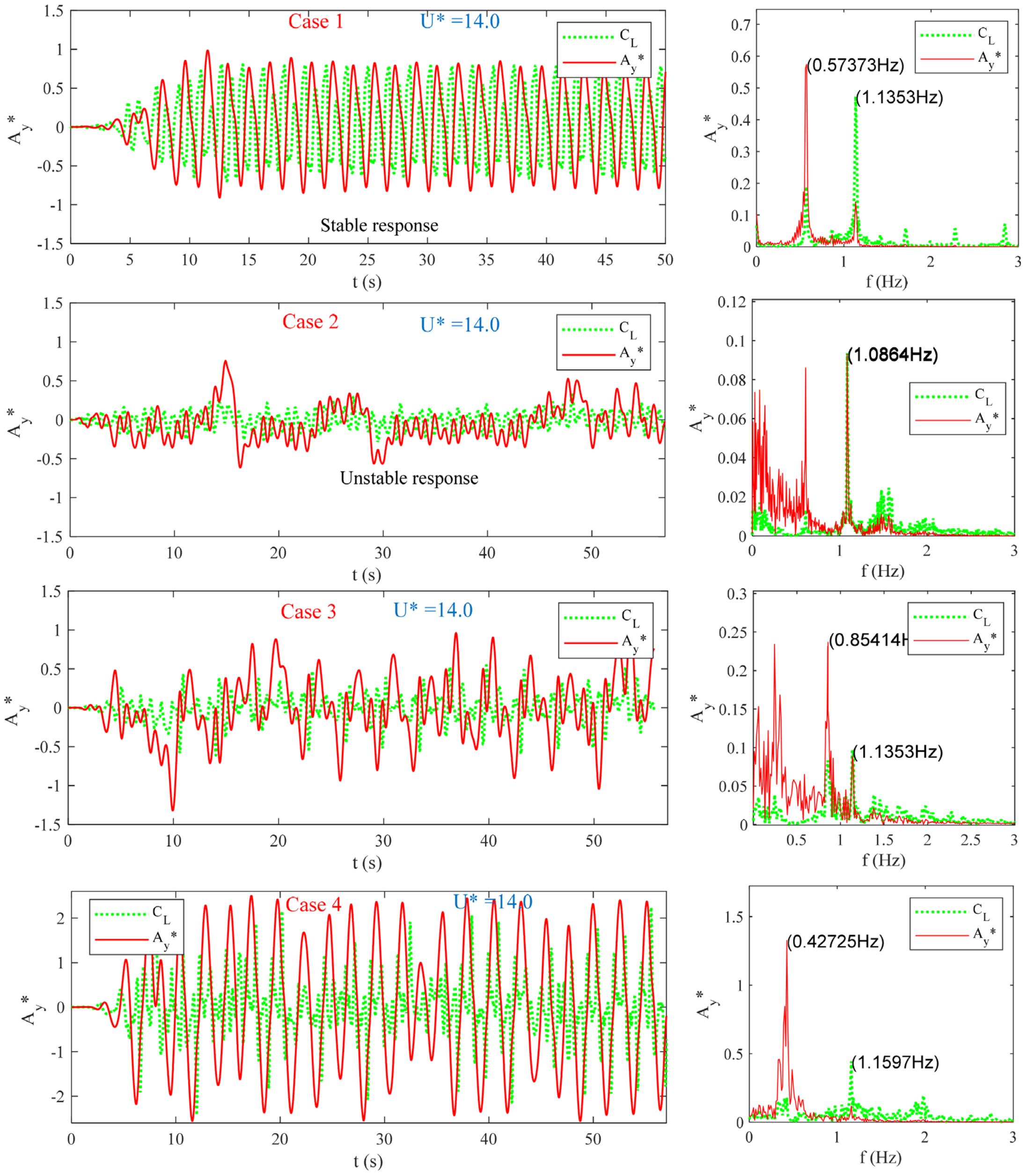

FIG. 16. The time histories of VIV responses of the cylinder with different number of the grooves ($U* = 14.0$).

cases 1, 2, 3, and 4, when the cylinder is located at the upper limit of the cross-flow vibration. The cylinders of cases 1 and 4 have very similar pressure distributions. On the right side of the vibration cylinder are large low-pressure areas; among them, the low-pressure area of case 4 is lager. Between two cylinders have high-pressure areas. For cases 2 and 3, the right side of the vibration cylinders is smaller low-pressure areas compared with case 1.

The injection momentum from the jet to the cylinder boundary layer and shear layer in cases 2 and 3 results in a reduction of length and width for the low-pressure areas located behind the vibration cylinder. On the other hand, in case 4, it can be observed that the area of low pressure behind the vibrating cylinder is expanded, suggesting that injection has an adverse impact under these circumstances. Hence, the utilization of jet control proves to be more efficient in minimizing drag and lift for the cylinder when it is positioned at smaller angles.

In conjunction with polar Fig. 20, pressure distributions on the cylinders about cases 2 and 4 are given when the cylinders are located at the upper limit of the cross-flow vibration. At this point, the motion direction of the cylinders is upward along the cross-flow. For case 4, a

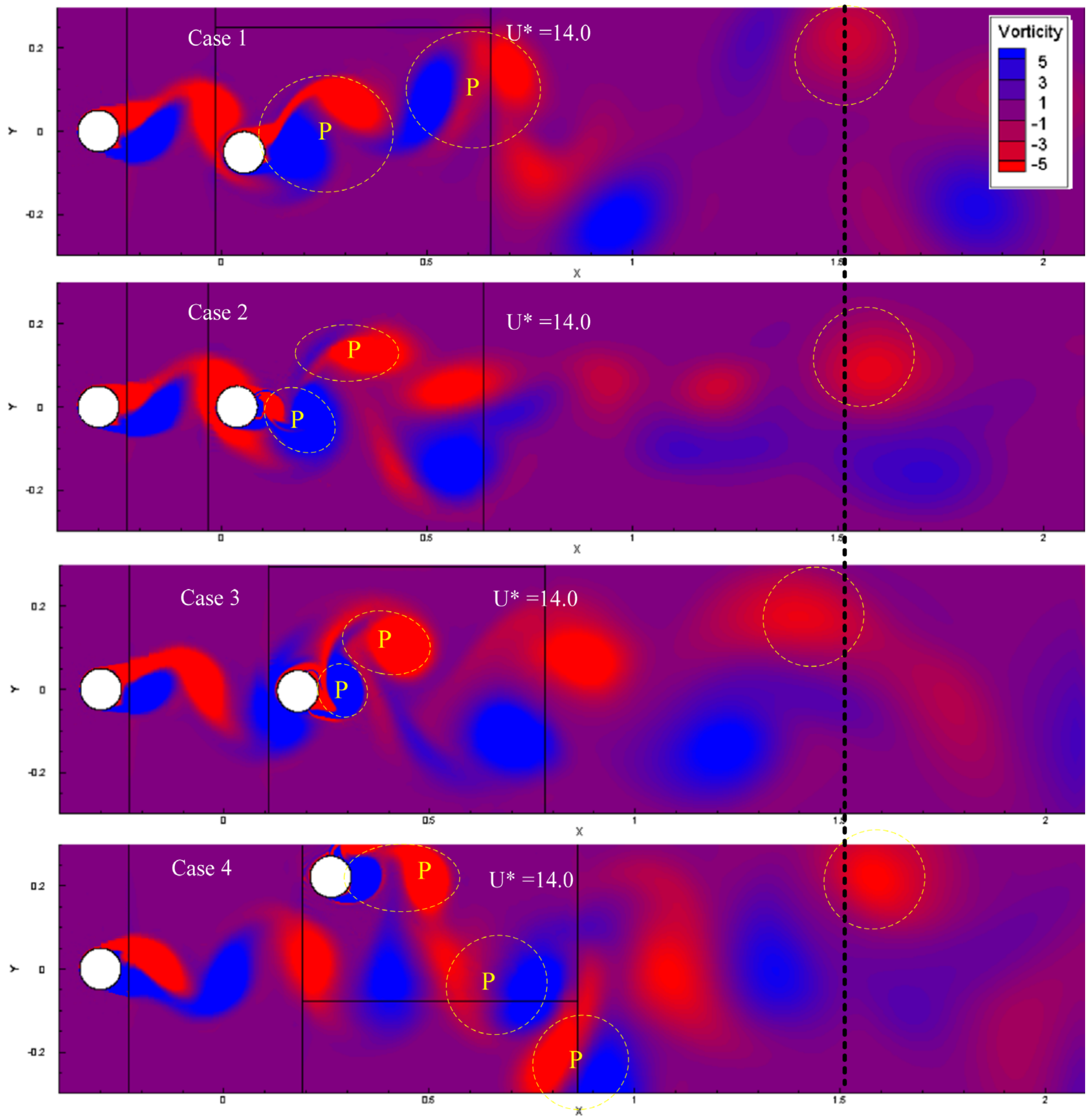

FIG. 17. The vortex patterns of the cylinders ($U* = 14.0$).

low-pressure area still exists behind the jet (polar coordinates are 30°–90°), and there is a high-pressure area in the 180°–270° range. Therefore, there is a large pressure difference around the cylinder during the upward movement phase, which provides the impetus for the upward movement of the cylinders, resulting in a relatively high amplitude of vibration. In contrast, for case 2, the red line around the cylinder is fuller, which provides a smaller pressure difference in the direction of motion, resulting in less driving force.

B. Flow structure around the cylinders

The main reason for vortex shedding is the large-scale boundary layer separation. The aim is to further investigate the suppression mechanism of cylindrical wake vibration using the jet. During fluid flow, vortices and shear layers are formed when the flow velocity exceeds a certain critical velocity. When the alternating vortices and shear layers interact with the surface of the structure, vibration of the structure will be generated. It has been shown that the vortices shed by the upstream cylinder will gradually merge into the vortices around the downstream cylinder and thus significantly enhance the vibration of the downstream cylinder.[32,46,47] When the cylinder approaches the limited point and the middle point, the velocity and vorticity contours at $U^* = 7.0$ and $\beta = 30°$ are given in Fig. 21. After the separation of the boundary layer, a vortex with low pressure will be generated in the wake of the cylinder. Due to the occurrence of boundary layer separation on both the upper and lower walls of the cylinder, two vortexes

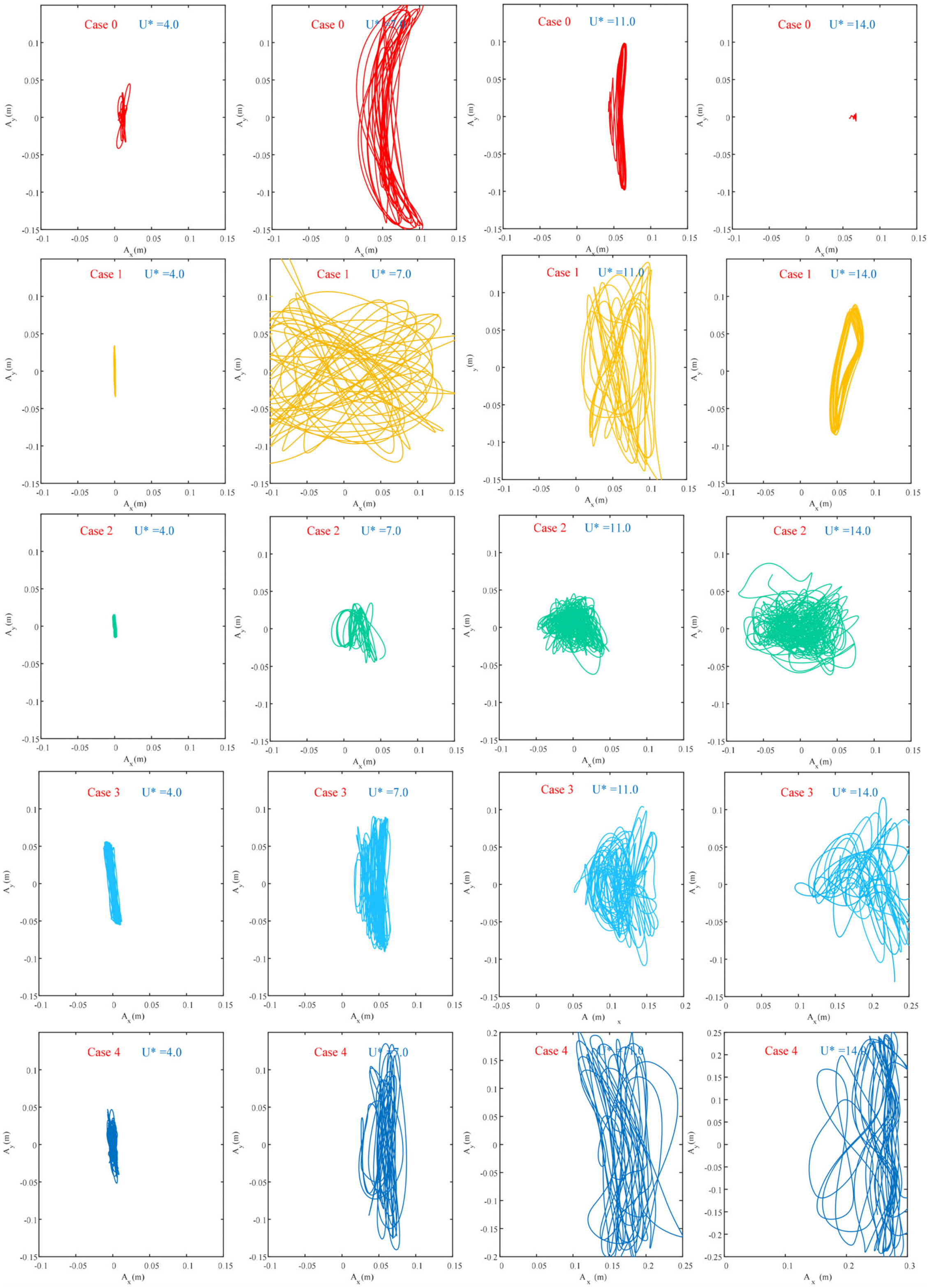

FIG. 18. The 2-DOF trajectories of the cylinders.

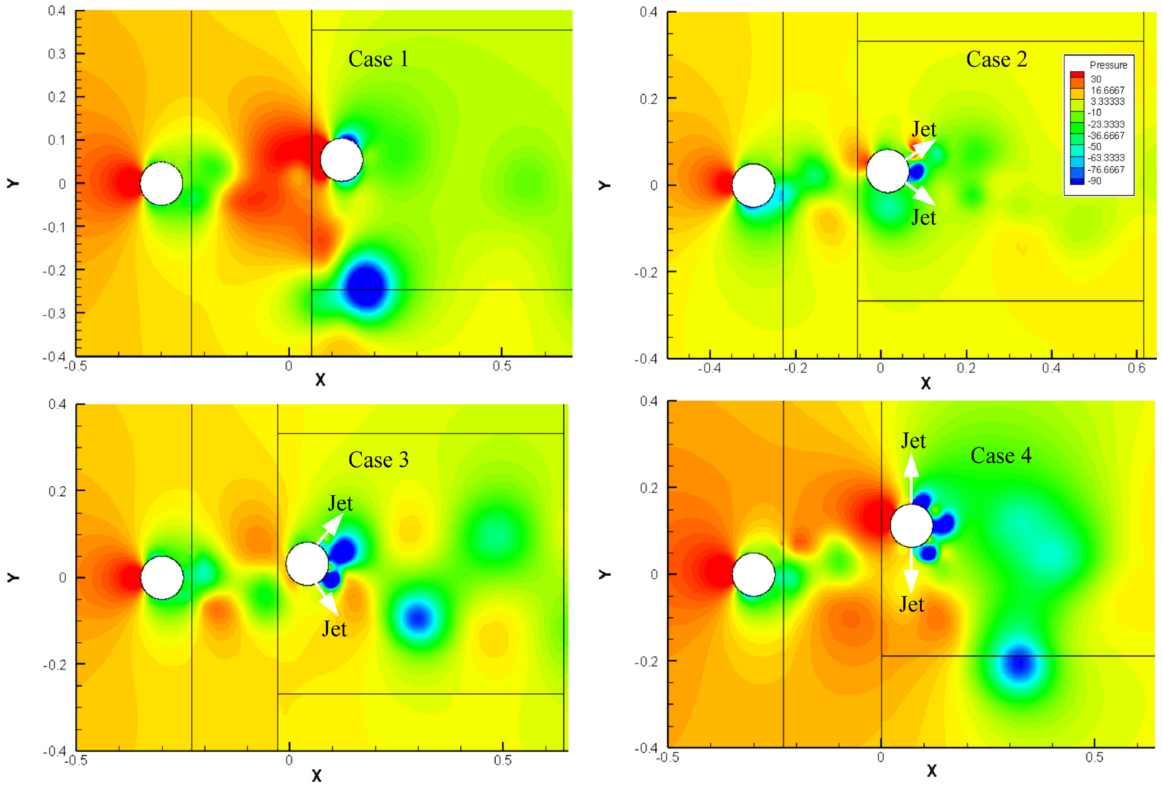

FIG. 19. The pressure contours around the cylinders ($U* = 7.0$).

will be shed in opposite directions. As can be seen from the figure, the size of the vortexes distributed behind the vibrating cylinder is all small. For the single cylinder, the same phenomenon was found by Zhu *et al.*[24] and Wang *et al.*[47] Generally, vortex generation is unavoidable, so breaking up large vortices is the main form of suppression VIV. Thus, the jet shreds the large shedding vortexes and thus reduce the vortex effect on the cylinders.

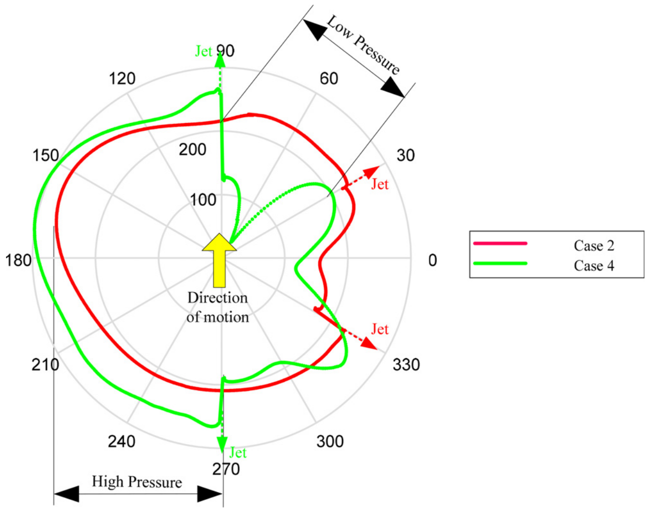

FIG. 20. Pressure distribution on the cylinders in the upward journey (case 2: $\beta = 30°$ and case 4: $\beta = 90°$).

In Fig. 22, due to the jet being implemented on the up shoulder of the vibration cylinder, the vortex (blue area) generated by the jet is opposite to the big vortex (red area) near itself. Similarly, the jet on the down shoulder works in the same way. Figure 22 is a schematic diagram of the structure where vortex shedding occurs around the cylinders. As the jet shreds the large vortex behind the cylinder, it results in a reduction of the cylinder driving force vibration, leading to the cylinder in the wake being significantly suppressed.

VI. CONCLUSIONS

This work studies an active vibration suppression method with jets for the cylinder. A series of simulations in conjunction with the Newmark-β method are carried out to research the vibration response of a two-degree-of-freedom cylinder. The simulation results are verified by comparing them with other studies. The WIV characteristics for four different conditions (uncontrolled, $\beta = 30°$, $\beta = 60°$, and $\beta = 90°$) are discussed in detail. The main conclusions are as follows:

(1) When the reduced velocity U^* ranges from 2 to 15, the amplitude response can be categorized into the initial branch, the upper branch, the lower branch, and the desynchronization region. The maximum CFAR decreases from 0.9 (case 1, uncontrolled) to 0.5 (case 2, $\beta = 30°$), a decrease of approximately

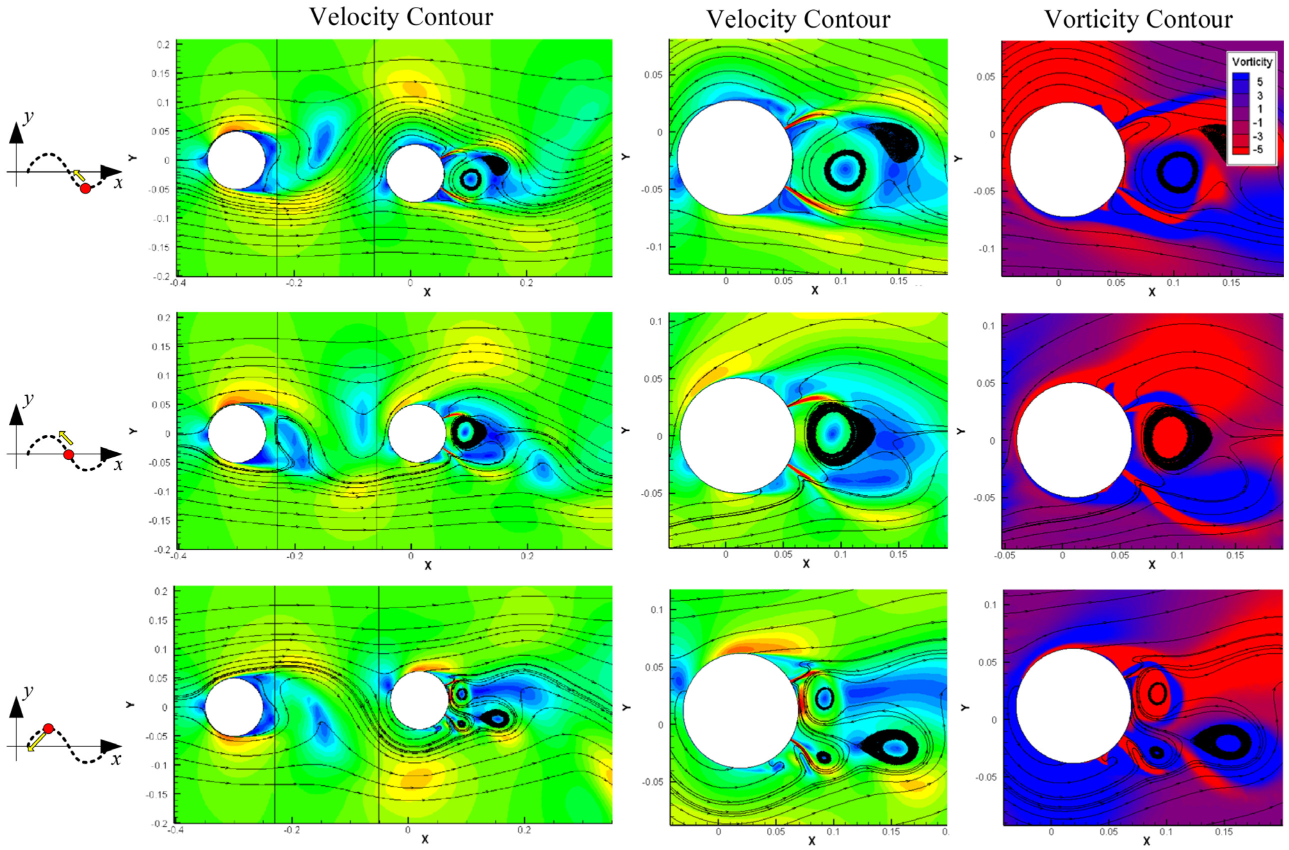

FIG. 21. Velocity and vorticity contours around the cylinder when approaching the highest point and the middle point ($U* = 7.0$).

44%. This indicates that the jets with $\beta = 30°$ are effective in reducing WIV amplitudes. On the contrary, the maximum CFARs are approximately 1.0 in case 3 ($\beta = 60°$) and case 4 ($\beta = 90°$), which are slightly higher than case 1 (uncontrolled). Of course, the response of case 3 is suppressed in the lower branch region. For case 4, after the upper branch, the cylinder enters the galloping response. At this moment, the jets have the effect of promoting vibration.

(2) The response of the cylinder's WIV is significantly suppressed when the jet angle β is 30° (case 2). The WIV frequency of case 2 is close to the shedding frequency of vortexes, and the cross-flow amplitude is relatively low and stable. However, the WIV frequencies of cases 1, 3, and 4 are closer to the natural frequency.

(3) The vortex pattern of case 1 (uncontrolled) switches from 2S to 2P as the reduced velocity increases. The vortex pattern (2P) of case 2 ($\beta = 30°$) and case 3 ($\beta = 60°$) remains unchanged. As the reduced velocity increases, the vortex pattern of case 4 ($\beta = 90°$) switches from 2P to 4P.

(4) Compared to the pressure contour of case 1 (uncontrolled) and case 4 ($\beta = 90°$), the area of low-pressure vortexes around case 2 ($\beta = 30°$) and case 3 ($\beta = 60°$) is smaller. Especially for case 2, the pressure curve around the cylinder is fuller, which results in less pressure difference in the direction of motion. Therefore, the driving force of cylinder vibration is smaller. The cylinder's response is significantly diminished. Due to jets set on the vibration cylinder, the vortexes generated by the jet are opposite to big vortexes near itself. Therefore, the water jet shreds the large vortex behind the cylinder, which results in the driving force of the cylinder vibration reducing and significant suppression of the cylinder in the wake.

The control effect of active suppression on vibration is indeed ideal, but there is still a lot of progress to be made in the technology of realizing vibration control by water jets. In general, the velocity of the

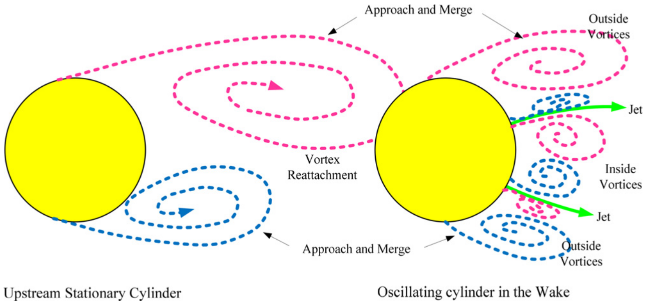

FIG. 22. Schematic diagrams of vortex shedding structure around the cylinders.

ocean current is not constant in the marine environment. Different water jet velocities are suitable for different current environments. Therefore, an adaptive water jet control system can be studied. The main direction of parameter selection can refer to the ocean current velocity, the vibration direction, the angle of the jet, and so on. Adaptive feedback system is an ideal research direction in the future.

ACKNOWLEDGMENTS

This project was funded by the National Natural Science Foundation of China (Nos. 52201327, 52272360, and 52005288).

AUTHOR DECLARATIONS

Conflict of Interest

The authors have no conflicts to disclose.

Author Contributions

Baoshou Zhang: Formal analysis (equal); Investigation (equal); Writing – original draft (equal). **Teng Long:** Methodology (equal). **Ziyu Wang:** Investigation (equal). **Wei Wang:** Conceptualization (equal); Resources (equal). **Boyang Li:** Formal analysis (equal). **Renhe Shi:** Formal analysis (equal).

DATA AVAILABILITY

The data that support the findings of this study are available within the article.

REFERENCES

[1] D. Sumner and H. K. Reitenbach, "Wake interference effects for two finite cylinders: A brief review and some new measurements," J. Fluids Struct. **89**, 25–38 (2019).

[2] P. Hishikar, S. K. Dhiman, A. K. Tiwari *et al.*, "Analysis of flow characteristics of two circular cylinders in cross-flow with varying Reynolds number: A review," J. Therm. Anal. Calorim. **147**, 5549–5574 (2022).

[3] R. Chen, Y. Yuan, and D. Thomson, "A review of mathematical modelling techniques for advanced rotorcraft configurations," Prog. Aerosp. Sci. **120**, 100681 (2021).

[4] D. Sumner, "Two circular cylinders in cross-flow: A review," J. Fluids Struct. **26**, 849–899 (2010).

[5] A. Teimourian, S. Yazdi, and H. Hacisevki, "Vortex shedding: A review on flat plate," Fluid Dyn. **53**(2), 212–221 (2018).

[6] W. Wang, Z. Mao, B. Song *et al.*, "Vortex-induced vibration response of a cactus-inspired cylinder near a stationary wall," Phys. Fluids **33**, 077119 (2021).

[7] W. Wang, Z. Mao, B. Song *et al.*, "Suppression of vortex-induced vibration of a cactus-inspired cylinder near a free surface," Phys. Fluids **33**, 067103 (2021).

[8] W. Wang and Z. Mao, "Numerical investigation on vortex-induced vibration suppression of the cactus-inspired cylinder with some ribs," Phys. Fluids **33**, 037127 (2021).

[9] J. S. Wang, D. Fan, and K. Lin, "A review on flow-induced vibration of offshore circular cylinders," J. Hydrodyn. **32**, 415–440 (2020).

[10] P. S. Balaji and K. Karthik SelvaKumar, "Applications of nonlinearity in passive vibration control: A review," J. Vib. Eng. Technol. **9**, 183–213 (2021).

[11] W. Wang, B. Song, Z. Mao *et al.*, "Numerical investigation on VIV suppression of the cylinder with the bionic surface inspired by giant cactus," Ocean Eng. **214**, 107775 (2020).

[12] C.-C. Chang, R. Ajith Kumar, and M. M. Bernitsas, "VIV and galloping of single circular cylinder with surface roughness at $3.0 \times 10^4 < \mathrm{Re} < 1.2 \times 10^5$," Ocean Eng. **38**, 1713–1732 (2011).

[13] M. Ozkan Gokturk, V. Oruc, H. Akilli *et al.*, "Flow around a cylinder surrounded by a permeable cylinder in shallow water," Exp. Fluids **53**(6), 1751–1763 (2012).

[14] G. Yun, F. Shixiao, M. Leixin *et al.*, "Experimental investigation of the response performance of VIV on a flexible riser with helical strakes," Ships Offshore Struct. **11**(2), 113–128 (2016).

[15] Y. Gao, S. Fu, T. Ren *et al.*, "VIV response of a long flexible riser fitted with strakes in uniform and linearly sheared currents," Appl. Ocean Res. **52**, 102–114 (2015).

[16] Y. Sun, J. Wang, S. Liang *et al.*, "Flow-induced vibration of a cylinder attached with a fishtail-like fairing using wind tunnel experiments," Ocean Eng. **237**, 109599 (2021).

[17] Y. Amini and I. Zahed, "Flow-induced vibration of two tandemly arranged circular cylinders with attached splitter plates," Ocean Eng. **237**, 109604 (2021).

[18] F. Ren, C. Wang, and H. Tang, "Active control of vortex-induced vibration of a circular cylinder using machine learning," Phys. Fluids **31**, 093601 (2019).

[19] C. E. N. Mazzilli and C. T. Sanches, "Active control of vortex-induced vibrations in offshore catenary risers: A nonlinear normal mode approach," J. Mech. Mater. Struct. **6**(7–8), 1079–1088 (2011).

[20] H. Wan and S. S. Patnaik, "Suppression of vortex-induced vibration of a circular cylinder using thermal effects," Phys. Fluids **28**, 123603 (2016).

[21] M. Lou, Y. Wang, G. Qian *et al.*, "Investigation on the vortex-induced vibration active control of the riser in the "lock-in" region based on adaptive fuzzy sliding mode theory," Ocean Eng. **238**, 109697 (2021).

[22] F. Xie, H. Zheng, J. Deng *et al.*, "Vortex induced vibration of a circular cylinder with a filament by using penalty immersed boundary method," Ocean Eng. **186**, 106078 (2019).

[23] A. Chizfahm and R. Jaiman, "Data-driven stability analysis and near-wake jet control for the vortex-induced vibration of a sphere," Phys. Fluids **33**, 044104 (2021).

[24] H. Zhu, T. Tang, H. Zhao *et al.*, "Control of vortex-induced vibration of a circular cylinder using a pair of air jets at low Reynolds number," Phys. Fluids **31**, 043603 (2019).

[25] H. Zhu, T. Tang, and Z. Honglei, "Modification of wake flow and air-bubble-vortex interference in the flow control of a circular cylinder with a pair of air jets: Effect of injection velocity," Ocean Eng. **214**, 107766 (2020).

[26] J. Kim and H. Choi, "Distributed forcing of flow over a circular cylinder," Phys. Fluids **17**, 033103 (2005).

[27] C. Wang, H. Tang, S. C. M. Yu *et al.*, "Control of vortex-induced vibration using a pair of synthetic jets: Influence of active lock-on," Phys. Fluids **29**, 083602 (2017).

[28] J. Wang, Y. Zhang, G. Hu, and W. Zhang, "Wake-induced vibration and heat transfer characteristics of three tandem semi-circular cylinders," J. Fluids Struct. **123**, 104004 (2023).

[29] R. Tang, Y. Gu, X. Mi, D. Yurchenko, F. Xu, W. Xu, X. Liu, and J. Wang, "Numerical analysis of WIV phenomenon with two in-series cylinders: WIV suppression and energy harvesting," Ocean Eng. **262**, 112154 (2022).

[30] C. Dongyang, L. K. Abbas, W. Guoping, R. Xiaoting, and P. Marzocca, "Numerical study of flow-induced vibrations of cylinders under the action of nonlinear energy sinks (NESs)," Nonlinear Dyn. **94**, 925–957 (2018).

[31] W. Xu, Y. Li, K. Jia, and Q. Wang, "Performance of helical strakes in suppressing the FIV fatigue damage of two long flexible cylinders in a tandem configuration," Ocean Eng. **239**, 109836 (2021).

[32] B. Zhang, Z. Mao, L. Wang *et al.*, "A novel V-shaped layout method for VIV hydrokinetic energy converters inspired by geese flying in a V-formation," Energy **230**, 120811 (2021).

[33] M. Gu, B. Song, B. Zhang *et al.*, "The effects of submergence depth on vortex-induced vibration (VIV) and energy harvesting of a circular cylinder," Renewable Energy **151**, 931–945 (2020).

[34] M. H. Wu, C. Y. Wen, R. H. Yen *et al.*, "Experimental and numerical study of the separation angle for flow around a circular cylinder at low Reynolds number," J. Fluid Mech. **515**, 233–260 (2004).

[35] B. S. Zhang, B. W. Song, Z. Y. Mao, W. L. Tian, and B. Y. Li, "Numerical investigation on VIV energy harvesting of bluff bodies with different cross sections in tandem arrangement," Energy **133**, 723–736 (2017).

[36] B. S. Zhang, Z. Y. Mao, B. W. Song, W. J. Ding, and W. L. Tian, "Numerical investigation on effect of damping-ratio and mass-ratio on energy harnessing of a square cylinder in FIM," Energy **144**, 218–231 (2018).

[37]N. M. Newmark, "A method of computation for structural dynamics," J. Eng. Mech. Div. **85**(3), 67–94 (1959).
[38]J.-F. Deü and D. Matignon, "Simulation of fractionally damped mechanical systems by means of a Newmark-diffusive scheme," Comput. Math. Appl. **59**(5), 1745–1753 (2010).
[39]D. Xiaolong, "Numerical simulation of vortex induced vibration s using PCNewmark-B-based fluid-structure interaction method," Ph.D. dissertation (Zhejiang University, 2015).
[40]B. S. Zhang, B. W. Song, Z. Y. Mao, B. Y. Li, and M. F. Gu, "Hydrokinetic energy harnessing by spring-mounted oscillators in FIM with different cross sections: From triangle to circle," Energy **189**, 116249 (2019).
[41]Z. Y. Li, H. B. Hu, C. Wang *et al.*, "Hydrodynamics and stability of oblique water entry in waves," Ocean Eng. **292**, 116506 (2024).
[42]B. Y. Li, Y. J. Zhong, B. S. Zhang *et al.*, "Effect of a rotatable water-drop plate on vortex-induced vibration of cylinder," Ocean Eng. **292**, 116558 (2024).
[43]W. Wang, B. Song, Z. Mao *et al.*, "Numerical investigation on vortex-induced vibration of bluff bodies with different rear edges," Ocean Eng. **197**, 106871 (2020).
[44]N. Jauvtis and C. H. K. Williamson, "The effect of two degrees of freedom on vortex-induced vibration at low mass and damping," J. Fluid. Mech **509**, 23–62 (2004).
[45]Z. Kang, C. Cheng, and G. Ma, "A numerical investigation of the effects of Reynolds number on vortex-induced vibration of the cylinders with different mass ratios and frequency ratios," Int. J. Nav. Arch. Ocean **11**(2), 835–850 (2019).
[46]B. Zhang, B. Li, C. Li, H. Yu, D. Wang, and R. Shi, "Effects of variable damping on hydrokinetic energy conversion of a cylinder using wake-induced vibration," Renewable Energy **213**, 176–194 (2023).
[47]H. Wang, L. Ding, L. Zhang, R. N. Sharma, and L. Yang, "Numerical study on two-degree-of-freedom vortex induced vibrations suppression of a circular cylinder via synthetic jets at different excitation frequencies," Int. J. Heat Fluid Flow **84**, 108593 (2020).